

Chapter 2

COMPUTATIONAL FRAMEWORK

Paul M. Meaney, Ph.D. and Keith Paulsen, Ph.D.

1 INTRODUCTION

All of the imaging modalities discussed in this book require unique numerical algorithms and data acquisition hardware. However, they also share a good deal of algorithmic common ground. The Dartmouth Breast Imaging Group has therefore articulated a shared numerical-analysis framework for these modalities. This framework facilitates communication between teams working on different modalities while being flexible enough to allow for needful variations, especially as dictated by the data-acquisition requirements of each modality.

In all four modalities, imaging requires the solution of an inverse problem. That is, measurements are made of some physical process (e.g., microwaves, infrared light, or mechanical vibrations) that interacts with the tissue, and from these external recordings the two- or three-dimensional distribution of physical properties of the tissue (dielectric properties, optical absorption coefficient, elasticity) is estimated using numerical algorithms.

The imaging strategies used by three of the modalities—electrical impedance spectroscopy (EIS), microwave imaging spectroscopy (MIS), and near-infrared spectroscopic imaging (NIS)—resemble those of x-ray computed tomography (CT). That is, they collect data with an array of detectors positioned around a central target while illuminating the target successively from all directions. The fourth modality, magnetic resonance elastography (MRE), is distinctly nontomographic in that it excites the whole tissue volume using a piezoelectric-based mechanical vibration system and collects

displacement information at each voxel within the target using magnetic resonance imaging techniques.

Because x-rays propagate in nearly straight lines through tissue, in CT an attenuation coefficient can be assigned directly to each pixel. The inverse solution for these attenuation coefficients requires only linear matrix operations. For the imaging modalities treated in this book, however, the inverse problem is nonlinear, because the physical interactions do not occur along straight lines but rather are distributed essentially throughout the imaging field-of-view. As a result, the measured response is not a linear function of tissue properties and iterative numerical methods are required to solve the inversion problem.

We have chosen to apply a well-known iterative technique, the Gauss-Newton method, to the solution of this suite of nonlinear inverse problems [1]. We estimate the spatial distribution of the tissue's physical properties; calculate the response that *would* be observed, given this distribution (i.e., solve the “forward problem”); compare these calculated observations to the actual data; and update the estimated property distribution accordingly. This process is iterated until the real and calculated observations converge, whereupon the estimated distribution is taken as the desired image.

2 FORWARD PROBLEM

2.1 Field Equations

Our finite-element approach requires that the measurable physical phenomenon of interest (e.g., electromagnetic waves) must be governed by a partial differential equation. Listed below are the model equations for the four modalities, along with the tissue properties associated with the measurable responses.

1. *Helmholtz wave equation* (MIS). For sinusoidal electromagnetic waves in source-free regions, Maxwell's equations reduce to the homogeneous Helmholtz wave equations [2]. In particular, the electric-field component \mathbf{E} of a sinusoidal electromagnetic wave obeys

$$\nabla^2 \mathbf{E} + k^2 \mathbf{E} = 0 \quad (2.1)$$

Here $k^2 = \omega^2 \mu \epsilon + j\omega \mu \sigma$, where k is the wave number, ω is radian frequency, $j = \sqrt{-1}$, and the medium is characterized by magnetic permeability μ , electrical permittivity ϵ , and conductivity σ . In media with nonuniform

electrical properties (e.g., tissue), k^2 varies locally. Its spatial variation throughout the breast is the quantity we are interested in imaging in MIS.

2. *Diffusion equation* (NIS). The diffusion equation for an absorptive, scattering, linearly anisotropic optical medium is

$$-\nabla \cdot D \nabla \Phi + \left(\mu_a + j \frac{\omega}{c_m} \right) \Phi = q_0 \quad (2.2)$$

where Φ is the photon fluence, c_m is the speed of light in the medium, q_0 is the intensity of an isotropic light source, and D is the diffusion coefficient, which is a function of the absorption and reduced scattering coefficients μ_a and μ'_s , i.e., $D = 1/[3(\mu_a + \mu'_s)]$. The diffusion coefficient is the locally-varying physical quantity of interest in this modality.

3. *Laplace's equation* (EIS). In any charge-free region in a dielectric medium, the voltage (potential) at every point is governed by Laplace's equation:

$$\nabla \cdot (\sigma + j\omega\epsilon) \nabla \Psi = 0 \quad (2.3)$$

Here, Ψ is the voltage and the medium has electrical permittivity ϵ and conductivity σ . Laplace's equation is an appropriate relationship for EIS because the EIS system operates at frequencies several orders of magnitude below those used by the MIS system (a realm where the Helmholtz equation applies). As in MIS, the electrical properties of the tissue (ϵ and σ) are the physical quantities of interest.

4. *Navier's equation* (MRE). The governing differential relationship for the MRE modality is Navier's equation, which is in essence a multidimensional generalization of Hooke's Law of linear elasticity. Navier's equation describes the displacement field inside an elastic body subject throughout to stress and strain as follows:

$$\nabla \cdot \mu \nabla \mathbf{u} + \nabla(\lambda + \mu) \nabla \cdot \mathbf{u} = \rho \frac{\partial^2 \mathbf{u}}{\partial t^2} \quad (2.4)$$

Here, the three-dimensional vector \mathbf{u} represents displacement within the medium, μ and λ are the material stiffness moduli known as Lamé's constants

(presumed here to vary throughout the medium as scalar fields), and ρ is the density. The properties of interest are the moduli μ and λ (and possibly ρ).

For all modalities we have focused on the frequency-domain version of the problem; that is, we have assumed a periodic time variation of the form $e^{-i\omega t}$ for all nonconstant quantities and have solved the resulting steady-state system. An equally valid time-domain solution could be obtained on identical FE meshes by modeling the evolution of the system through time, but we have chosen the frequency-domain approach for the three tomographic modalities (MIS, NIS, EIS) because of limitations imposed by hardware calibration procedures and the advantages of exploiting the frequency-dispersion characteristics of the propagating media.*

For MRE, likewise, data are acquired at only a single mechanical-excitation frequency. Acquiring data at multiple mechanical excitation frequencies is possible but would be time-consuming using current methods.

2.2 Numerical Solution Framework

There are a number of numerical approaches for computing the electromagnetic fields or mechanical displacements throughout an inhomogeneous medium. These include finite elements, finite differences, method of moments, finite-difference time domain, and others [3–6]. Each has merits, but the finite element (FE) method is particularly useful for our purposes.

The FE method approximates a continuous medium as a mesh of polygonal or polyhedral elements with shared vertices (the nodes of the mesh). These elements are usually triangular (in 2D problems) or tetrahedral (in 3D problems). A basis function is centered on each node, and the physical phenomenon of interest is modeled at every point in the region of interest as a weighted sum of these basis functions. For an N -node mesh, this entails the solution of a matrix equation of the form $[A]\{\Phi\}=\{b\}$, where $[A]$ is $N \times N$; however, because the basis function associated with each node is nonzero only over those finite elements which contain that node, $[A]$ is sparse (populated with zeroes except near the diagonal) and therefore amenable to iterative and/or banded-matrix solutions. This enables important efficiencies in storage and computation [7]. Furthermore, the nodes of an FE mesh can be placed arbitrarily, allowing accurate modeling of irregular ob-

* Time-domain signals could be synthetically derived from frequency data by fast Fourier transform if it could be collected at a sufficiently large number of fixed frequencies, but this would dramatically increase hardware complexity and data-acquisition time. Conversely, the full-spectrum frequency response could be obtained from time-domain data.

ject contours and increased node density in areas where the fields to be modeled vary rapidly [4].

In the two-dimensional case (readily generalizable to three dimensions), we consider the physical phenomenon of interest (i.e., waves propagating through the image region) as a scalar field, $\Phi(x, y)$ (readily generalizable to a vector field). $\Phi(x, y)$ is defined over an area covered by a mesh of finite elements (Figure 1).

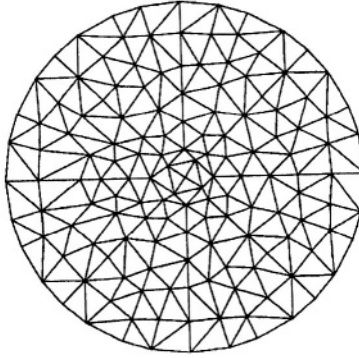


Figure 1. A two-dimensional finite-element mesh composed of several hundred triangular elements. In this particular mesh, each node (element vertex) is shared by as many as eight or as few as two elements.

Let $F[\Phi(x, y)] = 0$ be the differential equation (e.g., Laplace's) for which $\Phi(x, y)$ is the exact solution and for which some $\Phi_N(x, y)$, to be determined, is an *approximate* solution over an FE mesh having N nodes. $\Phi_N(x, y)$ is defined as the sum of N "basis functions," $\phi_i(x, y)$, that are weighted by N constants, Φ_i :

$$\Phi_N(x, y) = \sum_{i=1}^N \Phi_i \phi_i(x, y) \quad (2.5)$$

The $\phi_i(x, y)$ are known and the N coefficients Φ_i are unknown.

In general, $F[\Phi_N(x, y)] = R$, the nonzero "residual" or error that results from substituting $\Phi_N(x, y)$ for the exact solution $\Phi(x, y)$. To minimize R , that is, to find the best possible $\Phi_N(x, y)$, we use the *weighted residual* method (described in many textbooks on finite element methods, e.g., [4]). In this approach, R is multiplied by a chosen weighting function $w_j(x, y)$, the product $w_j(x, y)R$ is integrated over the domain of the entire FE mesh, Ω , and the result is set equal to zero:

$$\int_{\Omega} w_j(x, y) R \, dx \, dy = 0 \quad (2.6)$$

Substituting N different weighting functions $w_j(x, y)$ into (2.6) produces N equations in the N unknowns Φ_i .

Several simplifications can be made. First, each Lagrangian basis function $\phi_i(x, y)$ can be chosen to be nonzero only over those mesh elements of which the i th node is a vertex. Within each triangular finite element, therefore, only three $\phi_i(x, y)$ are nonzero and (2.5) simplifies to

$$\Phi_N(x, y) = \sum_{n=1}^3 \Phi_n \phi_n(x, y) \quad (2.7)$$

where n is a local index denoting the three vertices of the element, $\phi_n(x, y)$ is the basis function centered on node n , and Φ_n is the coefficient for $\phi_n(x, y)$ (see Figure 2).

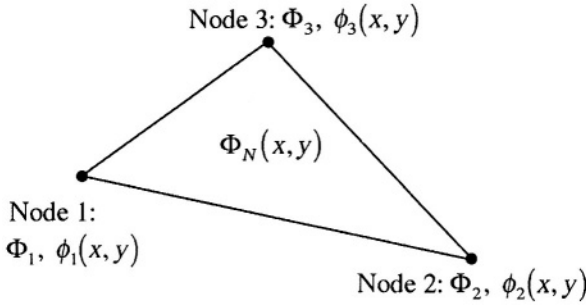


Figure 2. A triangular finite element. A coefficient Φ_n and linear basis function $\phi_n(x, y)$ are associated with each node. Each $\phi_n(x, y)$ is nonzero over this element and over all other elements of which its node is a vertex.

Second, in our implementation each basis function ϕ_i is linear, decreasing from 1 at the i th node to 0 along the opposite edge of each element sharing that node. The basis function ϕ_i at any node i that is surrounded entirely by mesh elements (i.e., any node that is not an edge node) can thus be visualized as an irregular pyramid with its peak over node i and its faces sloping down to the distal edges of all the elements sharing the node (Figure 3).

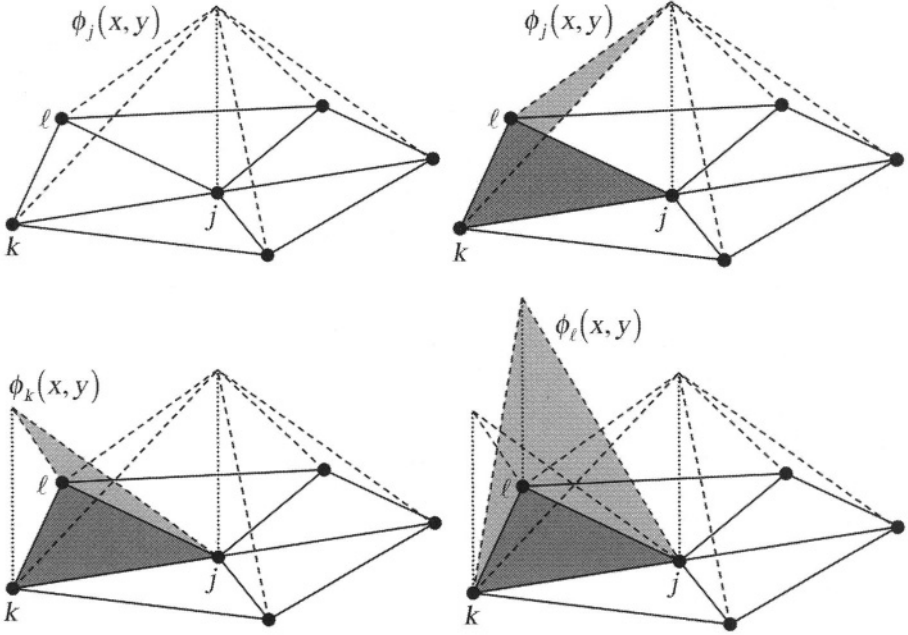


Figure 3. Relationship of piecewise-linear basis functions to triangular FE mesh elements. *Top left:* $\phi_j(x, y)$, the piecewise-linear basis function that is centered at node j , is shown over its whole domain (in this case, five elements). Its peak value is 1. *Top right:* The portion of $\phi_j(x, y)$ that overlaps element $jk\ell$ (dark gray). *Bottom left:* The portion of $\phi_k(x, y)$ that overlaps element $jk\ell$. *Bottom right:* The portion of $\phi_\ell(x, y)$ that overlaps element $jk\ell$. All other basis functions are zero over this element.

Third, the N basis functions ϕ_i used to form $\Phi_N(x, y)$ in (2.5) are employed as the N weighting functions w_i . When the weighting functions are equal to the basis functions, the resulting weighted-residuals method is termed the *Galerkin method*.

The presence of a Laplacian term (i.e., a second-order derivative) in the partial differential equation for each modality presents difficulties, since the basis functions are linear. That is, wherever a Laplacian term appears in the governing equation, it generates

$$\nabla^2 \Phi_N = \nabla^2 \left(\sum_{i=1}^N \Phi_i \phi_i \right) = \sum_{i=1}^N \Phi_i \nabla^2 \phi_i \quad (2.8)$$

in the residual R , and $\nabla^2 \phi_i = 0$ for linear ϕ_i on the element interior. (Technically, (2.8) generates an integrable singularity at the boundaries between elements because of the discontinuity in $\nabla \phi_i$ at element interfaces.) The disappearance of all second-derivative terms from R can be resolved by generating a weak form of (2.6) that has lower continuity requirements on resulting derivative terms. When a basis function ϕ_j is used as the weighting function w_j in (2.6) (i.e., when the Galerkin method is used), second derivatives like those in (2.8) give rise to

$$\int_{\Omega} \phi_j \nabla^2 \phi_i \, dx \, dy \quad (2.9)$$

We apply Green's identity to (2.9). In the two-dimensional case, Green's identity states that for any two scalar functions u and v continuous on some domain Ω with boundary C ,

$$\int_{\Omega} u \nabla^2 v \, dx \, dy = \oint_C u \frac{\partial v}{\partial \mathbf{n}} \, dS - \int_{\Omega} \nabla u \cdot \nabla v \, dx \, dy \quad (2.10)$$

where dS is a differential segment of C and $\partial v / \partial \mathbf{n} = \nabla \phi_i \cdot \hat{\mathbf{n}}$ (i.e., the normal derivative) [4]. This yields

$$\langle \phi_j \nabla^2 \phi_i \rangle = \oint_C \frac{\partial \phi_i}{\partial \mathbf{n}} \phi_j \, dS - \langle \nabla \phi_i \cdot \nabla \phi_j \rangle \quad (2.11)$$

where $\langle \cdot \rangle$ designates integration over the problem domain Ω . (In the three-dimensional case, $\langle \cdot \rangle$ designates volume integration and the contour integral becomes a surface integral.) Equation (2.11) contains derivatives of at most first order in both integral terms, sidestepping the problem of vanishing (singular) second-order derivatives. Another advantage of (2.11) is the appearance of the boundary integral, which is represented in terms of the natural boundary conditions expressed as the flux of the field through the enclosing surface.

When forcing and boundary conditions are taken into account, the resulting set of N weighted integral equations can be written in matrix form as

$$[\mathbf{A}]\{\Phi\} = \{\mathbf{b}\} \quad (2.12)$$

Matrix $[A]$ is $N \times N$ and contains terms dependent on the governing equation. The vector of basis-function coefficients, $\{\Phi\} = \{\Phi_1, \Phi_2, \dots, \Phi_N\}$, is the quantity to be computed. The entries in $\{b\}$, which account for forcing functions (i.e., external inputs to the system) and boundary conditions, arise during evaluation of the contour integral in (2.11). Matrix $[A]$ is sparse due to the localized nature of the basis functions, lending itself to efficient matrix-factorization routines [8] and/or iterative solvers.

Boundary conditions vary among modalities. For instance, the NIS and EIS approaches utilize mixed boundary conditions with

$$\Phi = A + B \frac{\partial \Phi}{\partial \mathbf{n}} \quad (2.13)$$

Here, A and B are known constants and \mathbf{n} is the unit normal vector oriented outward at the boundary [9]. The MRE approach applies either a Dirichlet or Neumann boundary conditions, depending on the physics of the mechanical vibration apparatus being used [4]. The MIS approach eliminates the need for approximate radiation boundary conditions by implementing a hybrid element method in which the FE method described above is used for the imaging zone and a boundary element (BE) method is used for the surrounding medium (i.e., in the breast-imaging setup, a homogeneous liquid in which the breast is immersed) [10]. The methods used to cope with boundary conditions are discussed in detail in the chapters devoted to the individual imaging modalities.

3 INVERSE PROBLEM

3.1 Gauss-Newton Iteration

The forward solution described above computes the spatial variation of an external observable (e.g., electric field) based on a given tissue-property distribution, governing equation, boundary conditions, and source terms. The *inverse* solution estimates the property distribution given the governing equation, boundary conditions, source terms, and measurements of the external observable. For all modalities considered in this book, the forward problem is linear and the inverse problem nonlinear [1, 4]. That is, the tissue properties to be estimated depend nonlinearly on the observable.

We have pursued a Gauss-Newton iterative scheme for solution of the inverse problem [1]. This approach begins with an initial estimate of the

property distribution and solves the forward problem based on this initial distribution. It then compares this solution with the measured data (as specified below) and solves a linearized approximation of the inverse problem to obtain a new estimate of the property distribution. This procedure is iterative: the property-estimate updating is repeated until the algorithm converges to an optimal least-squares fit of modeled data to measured data.

We employ an iterative Newton algorithm defined by

$$\xi_{v+1} = \xi_v - (f'(\xi))^{-1} f(\xi) \quad (2.14)$$

Here, ξ_v is the estimate of the material property distribution at the v th iteration, ξ_{v+1} is the updated estimate, and $f'(\xi)$ is the derivative of $f(\xi)$ with respect to ξ [11]. The functional $f(\xi)$ is defined in terms of a cost function, G , that expresses the difference between the measured and modeled data at each iteration:

$$G = \min \|\Phi(\xi) - \Phi_m\|^2 \quad (2.15)$$

$$\text{and} \quad f(\xi) = \frac{\partial G}{\partial \xi} = 2(\Phi(\xi) - \Phi_m) \frac{\partial \Phi}{\partial \xi} \quad (2.16)$$

Here, vectors $\Phi(\xi)$ and Φ_m are the computed (i.e., forward-solution) and measured values, respectively, of the observable quantity of interest at the measurement sites. Both are $O_{IM} = N_E \times O_E$ long, where N_E is the number of different excitations and O_E is the number of measurement sites per observation. (For example, in an imaging region surrounded by 16 microwave antennas, one of which transmits at any given time while the others receive, $N_E = 16$, $O_E = 15$, and $O_{IM} = 240$.) Furthermore, vectors ξ_v , ξ_{v+1} , and $\Delta\xi = \xi_{v+1} - \xi_v$ are all L long, where L is the number of material parameter values to be reconstructed. L is not necessarily equal to N , the number of nodes in the mesh used to model the observable phenomenon of interest; see discussion of the dual mesh scheme in the next section.

Using (2.16) and the fact that $f'(\xi) = 2(\partial\Phi/\partial\xi)^2$ (if $\partial^2\Phi/\partial\xi^2$ is assumed small enough to neglect),

$$(f'(\xi))^{-1} f(\xi) = \left(\frac{\partial\Phi}{\partial\xi} \right)^{-1} (\Phi(\xi) - \Phi_m) \quad (2.17)$$

Matrix $\partial\Phi/\partial\xi$ is $(M \times O) \times L$ and is termed the Jacobian matrix, $[J]$. Inserting (2.17) into (2.14) and rearranging produces (in matrix notation)

$$[J]\{\Delta\xi\} = \{\Phi_m - \Phi(\xi)\} \quad (2.18)$$

where $\{\Delta\xi\} = \{\xi_{v+1}\} - \{\xi_v\}$. Multiplying both sides by $[J^T]$, we have

$$[J^T J]\{\Delta\xi\} = [J^T]\{\Phi_m - \Phi(\xi)\} \quad (2.19)$$

We wish to calculate the update vector $\{\Delta\xi\}$, which, with $\{\xi_v\}$, gives $\{\xi_{v+1}\}$ at the new iteration. The entries of $\{\Phi_m\}$ are known and the entries of $\{\Phi(\xi)\}$ are computed using $\{\xi_v\}$ by the forward-solution method described earlier. Therefore, the only term of (2.19) still needed is $[J]$. We obtain this by differentiating (2.12) with respect to ξ . Vector $\{b\}$ contains only boundary and forcing information; it is therefore not a function of ξ and $\{db/d\xi\} = 0$. After rearranging,

$$\begin{bmatrix} A \end{bmatrix} \begin{bmatrix} \frac{\partial\Phi}{\partial\xi} \end{bmatrix} = - \begin{bmatrix} \frac{\partial A}{\partial\xi} \end{bmatrix} \begin{bmatrix} \Phi(\xi) \end{bmatrix} \quad (2.20)$$

Furthermore, $[A]$ and $\{\Phi(\xi)\}$ are computed at each iteration as part of the forward solution. Thus, only $[\partial A/\partial\xi]$ is needed to solve (2.20) for $[\partial\Phi/\partial\xi] = [J]$. The details of computing $[\partial A/\partial\xi]$ and $[\partial\Phi/\partial\xi]$ differ among the imaging modalities (see [12] and other chapters in this book). In Section 3.3, a closer look is taken at the method used for one particular modality (MIS).

A few of the computational techniques required for the efficient solution of the inverse problem will now be discussed, including the dual mesh scheme, the adjoint technique, and zone iterative reconstruction.

3.2 Dual Mesh Scheme

The system $[A]\{\Phi\} = \{b\}$ is rank N , but the dimension of the property distribution vector $\{\xi\}$ need not be N . We have exploited this fact to develop a *dual mesh* scheme [12].

In solving for the spatial distribution of the observable of interest in each modality, mesh discretization must be fine enough to meet accuracy criteria. For instance, in the MIS approach the nodes of the mesh must be separated by no more than approximately $\lambda/10$ (or one seventh of the exponential decay distance, whichever is less [13]). On the other hand, the spatial resolution required for $\{\xi\}$, which is directly related to the final image resolution, is dependent both on the spatial frequency of the parameter or parameters to be estimated (which is relatively low in all cases considered here) and on the amount of measurement data available. This points to a natural link between the amount of measurement data available and image resolution.

In the dual mesh method, the parameter ξ is represented on a mesh that is coincident with the forward-solution mesh but coarser. The nodes of this coarse mesh may be placed arbitrarily with respect to those of the mesh used for the forward solution of the observable phenomenon (Figure 4). Over each element of the L -node (“coarse” or “property”) mesh, ξ is defined as a weighted sum of Lagrangian basis functions analogous to that defining $\Phi_N(x, y)$ over the N -node (“fine” or “forward-solution”) mesh:

$$\xi(x, y) = \sum_{m=1}^L \xi_m \varphi_m(x, y) \quad (2.21)$$

Each φ_m , like each ϕ_i in (2.5), is a linear basis function that is nonzero only over its associated triangular elements; however, each φ_m is associated with a node of the coarse mesh, while each ϕ_i was associated with a node of the fine mesh. The summation in (2.21), like that in (2.7), only has three nonzero terms in two dimensions (four, in three dimensions) for any (x, y) in the area covered by the mesh element.

The dual mesh approach entails some computational overhead. For instance, in solving the forward problem, the property distribution must be mapped from the parameter mesh to the forward solution mesh. However, this is a linear operation that can be accomplished efficiently by matrix multiplication. As will be seen below, more significant computational overhead occurs in calculating the terms of the Jacobian matrix, $[\partial\Phi/\partial\xi]$.

As mentioned above, computing $[\partial\Phi/\partial\xi]$ differs among modalities. For illustrative purposes, the MIS case is considered here; the following equations are therefore specifically valid only when the governing equation is (2.1). More detailed treatments for each modality are provided in other chapters.

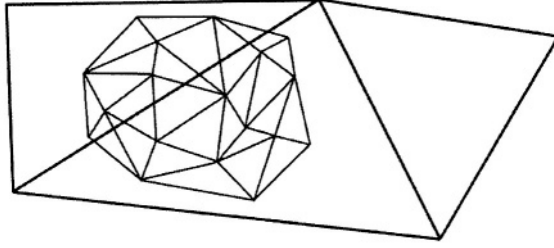


Figure 4. A portion of a parameter mesh (large triangles) with a portion of the forward-solution mesh (small triangles) that it overlays. In practice, the meshes are co-extensive.

We begin by examining the element at row i and column j of $[A]$ in (2.12):

$$\alpha_{i,j} = \langle \nabla \phi_i \cdot \nabla \phi_j \rangle + \langle \phi_i \phi_j \xi_i \rangle \quad (2.22)$$

The first term on the right-hand side results from multiplying the divergence operator in the Helmholtz equation by the weighting function ϕ_i and applying Green's identity to produce the weak-form solution. The second term results from multiplying $\xi(x, y)$ by ϕ_j and integrating over the model domain. (In the MIS case, ξ is equal to the wave number squared, k^2 .)

The next step in computing $[\partial \Phi / \partial \xi]$ is to differentiate $[A]$ with respect to ξ_ℓ , where ℓ denotes a node in the coarse mesh. This is accomplished by differentiating (2.22). (In principle, the calculation of L derivatives of $[A]$ is required, each an $N \times N$ matrix; however, as will be shown, only a few terms of each $[\partial A / \partial \xi_\ell]$ are nonzero.) Using the fact that neither ϕ_i nor ϕ_j is a function of ξ_ℓ and substituting for ξ_i from (2.21), differentiation of (2.22) gives

$$\begin{aligned} \frac{\partial \alpha_{i,j}}{\partial \xi_\ell} &= \frac{\partial \langle \nabla \phi_i \cdot \nabla \phi_j \rangle + \langle \phi_i \phi_j \xi_i \rangle}{\partial \xi_\ell} = \left\langle \phi_i \phi_j \frac{\partial \xi_i}{\partial \xi_\ell} \right\rangle \\ &= \left\langle \phi_i \phi_j \frac{\partial \left(\sum_{m=1}^L \xi_m \varphi_m \right)}{\partial \xi_\ell} \right\rangle = \langle \phi_i \phi_j \varphi_\ell \rangle \end{aligned} \quad (2.23)$$

where φ_ℓ is the basis function associated with node ℓ in the parameter mesh.

Although in principle each $\langle \phi_i \phi_j \varphi_\ell \rangle$ term requires integration over the entire fine-mesh area, its argument is nonzero only where φ_ℓ , ϕ_i , and ϕ_j are

all nonzero. That is, the integration in (2.23) need be performed only where those fine-mesh elements specified by the overlap of fine-mesh basis functions ϕ_i and ϕ_j are covered or masked by coarse-mesh basis function φ_ℓ . This means that the $N \times N$ matrix $[\partial A / \partial \xi_\ell]$ contains only a few nonzero elements, simplifying computation.

A minor complication arises whenever a fine-mesh element happens to straddle the boundary between two coarse-mesh elements (see Figure 3). In such a case, the argument of $\langle \phi_i \phi_j \varphi_\ell \rangle$ is nonzero over only *part* of that fine-mesh element, i.e., the part masked by φ_ℓ [12]. One might choose, when constructing the two meshes originally, to place their nodes so that each fine-mesh element resides entirely within one coarse-mesh element (no border-crossers). This would eliminate fragmentary element integrations but constrain mesh generation. Alternatively, one might allow arbitrary generation of both meshes and then perform fragmentary element integrations as needed. We have chosen the latter method [12]. The required procedures are computationally complex but not conceptually difficult.

The fact that $\partial \alpha_{i,j} / \partial \xi_\ell$ is a function only of the basis functions of the fine and coarse meshes offers large computational savings. Since the basis functions are a fixed feature of algorithm design, all nonzero elements of $[\partial A / \partial \xi_\ell]$ can be precalculated and stored in a lookup table, which saves the effort of recomputing them at each iteration.

3.3 Adjoint Method

A direct-differentiation technique for constructing the Jacobian matrix, which is used to solve for the property update vector $\{\Delta \xi\}$ at each iteration, was described in Section 3.1. However, this method can be computationally expensive. For instance, in a case where the forward-solution and parameter meshes have N and L nodes, respectively, and are surrounded by N_E source excitations, the computational load at each iteration includes (a) N_E LU factorizations of $[A]$ and N_E matrix back-substitutions for the forward problem and (b) $N_E \times L$ matrix back-substitutions for the inverse problem.

Little can be done to reduce the computational costs of the forward problem. However, in the inverse problem an alternative to direct computation of the Jacobian matrix is the *adjoint method* [14]. This is utilized in the NIS, EIS, and MIS modalities, where the principle of reciprocity can be exploited. Reciprocity holds where, for a fixed property distribution, the physical phenomenon measured at point r due to a given source at point s is equal to that which would be measured at s due to an equivalent source at r [15].

Interchangeability of image and source in lens optics is an example of reciprocity.

Each entry of the Jacobian matrix describes the change in the observable (e.g., electromagnetic field) corresponding to an infinitesimal property change at node ℓ in the coarse mesh, where the wave phenomenon is generated by a point source at location s and is measured at location r . Each entry in the Jacobian can thus be written as

$$\mathbf{J}_{s,r,\ell} = \left\langle \frac{\partial \Phi_s}{\partial \xi_\ell} \delta(x_r, y_r) \right\rangle \quad (2.24)$$

where Φ_s is the distribution of the observable resulting from a point source at s , δ is the Dirac delta function, x_r and y_r are the Cartesian coordinates of the measurement site r , and $\langle \cdot \rangle$ signifies integration over the region where ϕ_ℓ , the coarse-mesh basis function at node ℓ , is nonzero. Putting (2.24) aside for the moment, we rewrite (2.20) as

$$\left[\mathbf{A} \right] \left[\frac{\partial \Phi_s}{\partial \xi_\ell} \right] = - \left[\frac{\partial \mathbf{A}}{\partial \xi_\ell} \right] \left\{ \Phi_s \right\} = \left\{ \mathbf{b}_{eff} \right\} \quad (2.25)$$

Here, the right-hand side has been set equal to $\{\mathbf{b}_{eff}\}$, an “effective” source; that is, $\{\mathbf{b}_{eff}\}$ holds the same place in (2.25) as does the source term $\{\mathbf{b}\}$ in (2.12).

By reciprocity, if an auxiliary source $\{\mathbf{b}_r\}$ is (conceptually) placed at the receiver location r , the resulting observable $\{\Phi_r\}$ is found by solving

$$[\mathbf{A}]\{\Phi_r\} = \{\mathbf{b}_r\} \quad (2.26)$$

Here, each of the N entries of $\{\mathbf{b}_r\}$ is given by the inner product $\langle \phi_i V_r \rangle$, which is constructed by the process described in Section 2.2 (i.e., ϕ_i is the i th forward-mesh basis function employed as a weighting function). In agreement with assumption in (2.24) of a point source, V_r is chosen as

$$V_r = |V_r| \delta(x_r, y_r) \quad (2.27)$$

Combining (2.25) and (2.26) by reciprocity (and temporarily dropping matrix notation for simplicity), we obtain

$$\left\langle \mathbf{b}_r \frac{\partial \Phi_s}{\partial \xi_\ell} \right\rangle = \langle \mathbf{b}_{eff} \Phi_r \rangle \quad (2.28)$$

By (2.25), $\mathbf{b}_{eff} = -(\partial A / \partial \xi_\ell) \Phi_s$, where the (i, j) th element of $\partial A / \partial \xi_\ell$ is (as shown in the previous section) given by $\langle \phi_i \phi_j \varphi_\ell \rangle$. Substituting for terms on both sides of (2.28) thus yields, for a reciprocal point source \mathbf{b}_r ,

$$\left\langle |V_r| \delta(x_r, y_r) \frac{\partial \Phi_s}{\partial \xi_\ell} \right\rangle = - \left\langle \langle \phi_i \phi_j \varphi_\ell \rangle \Phi_r \Phi_s \right\rangle \quad (2.29)$$

Dividing both sides of (2.29) by $|V_r|$ produces

$$\left\langle \frac{\partial \Phi_s}{\partial \xi_\ell} \delta(x_r, y_r) \right\rangle = - \frac{1}{|V_r|} \left\langle \langle \phi_i \phi_j \varphi_\ell \rangle \Phi_r \Phi_s \right\rangle \quad (2.30)$$

The left-hand term, per (2.24), is $\mathbf{J}_{s,r,\ell}$. Since all values of $\langle \phi_i \phi_j \varphi_\ell \rangle$ can be stored as a precomputed weighting vector, each entry of the Jacobian can be computed during image reconstruction by means of a simple inner product of $\langle \Phi_s \Phi_r \rangle$ times a constant (i.e., $\langle \phi_i \phi_j \varphi_\ell \rangle / |V_r|$)—always providing that the sources and receivers are colocated, i.e., that each source antenna can also be configured to operate as a receiver. (In practice, many $\mathbf{J}_{s,r,\ell}$ need not be computed because $\langle \phi_i \phi_j \varphi_\ell \rangle$ is often zero.) This computation is an $O(N)$ operation, in contrast to the $O(N \times M)$ matrix back-substitutions in (2.20), where M is the bandwidth of the sparse matrix $[A]$. For large N , the savings can be significant. Finally, this approach is quite general and can be readily expanded to 3D for each modality.

3.4 Iterative Reconstruction in MRE

In the MRE system, tissue is vibrated along a single axis at low amplitude and low frequency. This excitation is phase-locked to the sequencing of the MR system to measure the harmonic displacement of each pixel in space. Because an information-rich volumetric data set is acquired in this case, strategies other than those described above (which exploit the fact that there are relatively few observations) must be utilized to improve computational efficiency. In the MRE case, the volumetric nature of the data allows dissection of the problem into multiple subzones, where the boundary conditions of each subzone are essentially the MR-measured displacements at each bound-

ary node. Coupling of these multiple subzone problems allows for accurate and efficient calculation of the inverse problem. The details of this approach are covered in Chapter 3, Sections 3–5.

4 ILL-CONDITIONING OF THE INVERSE PROBLEM

In all the approaches described above, the inverse problem is ill-conditioned. That is, the iterative procedure defined in (2.14)–(2.20) may not converge to a useful solution without the placement of additional restrictions on the process [16].

One way to assess ill-conditioning is to calculate the *condition number* of the Jacobian matrix, that is, the ratio of the largest eigenvalue of the system to the smallest [8]. As the condition number approaches or exceeds the numerical accuracy of the computer to be used, the system of equations is said to be unstable and the likelihood that the algorithm will converge diminishes. In effect, the system of equations is rank deficient and the amount of independent measurement information is not adequate.

Before discussing some of the standard mathematical approaches to ill-conditioning, it should be said that certain strategies can mitigate the problem without applying regularization methods. In general, adding more measurement data will improve the process, but it is not always clear how linearly independent the new data will be compared to the existing measurement set. In addition, the cost of adding new receiver channels can be high. Unwanted source and receiver interactions could be exacerbated by placing more receivers in an already crowded volume [17], and the added computational costs may be significant. However, there are important opportunities here. For instance, in all three tomographic approaches, data are acquired at multiple frequencies. Preliminary eigenvalue studies with the MIS system suggest that the inclusion of additional multifrequency data reduces the system condition number. Interestingly, depending on the individual system and on the orientation of sources and receivers, certain data (e.g., signals passing directly through the tissue versus signals diffracted to the sides) are clearly more valuable than others [18]. Finally, the problem statement itself can have a significant effect on the condition number. For instance, in the MIS system the eigenvalue spectral content is significantly improved when the minimization statement (2.15) starts from the log magnitude and phase form of the electric-field values rather than the more traditional complex form [18]. It has been shown that the former emphasizes the directly-transmitted data over the signals received by antennas close to the transmitter, and that the opposite

is the case for the complex-form algorithm. Attention to features other than regularization can thus be important.

4.1 Tikhonov Regularization

The most common approach to regularization is the Tikhonov method [16]. This approach begins with the minimization statement given in (2.15) and adds a weighted penalty term:

$$G = \min \left\| \Phi(\xi) - \Phi_m \right\|^2 + \rho \left\| \xi - \xi^* \right\|^2 \quad (2.31)$$

In this case, the penalized factor is a Euclidean distance term referenced to ξ^* with ρ as the weight. Other forms incorporate the first or second derivative of the property distribution. Now, $f(\xi)$ and its derivative $f'(\xi)$, referred to by (2.14), are given by

$$f(\xi) = \frac{\partial G}{\partial \xi} = 2(\Phi(\xi) - \Phi_m) \frac{\partial \Phi}{\partial \xi} + 2\rho(\xi - \xi^*) \quad (2.32)$$

$$\text{and} \quad f'(\xi) = 2 \frac{\partial \Phi}{\partial \xi} \frac{\partial \Phi}{\partial \xi} + 2\rho \quad (2.33)$$

where the second-order derivative of $\Phi(\xi)$ is ignored in determining $f'(\theta)$. Combining (2.14) and (2.33) yields

$$\Delta \xi = \left(\frac{\partial \Phi}{\partial \xi} \frac{\partial \Phi}{\partial \xi} + \rho \right)^{-1} \left[\frac{\partial \Phi}{\partial \xi} (\Phi_m - \Phi(\xi)) - \rho(\xi - \xi^*) \right] \quad (2.34)$$

This can be rewritten in matrix form as

$$[J^T J + \rho I] \{ \Delta \xi \} = [J^T] \{ \Phi_m - \Phi(\xi) \} - \rho \{ \xi - \xi^* \} \quad (2.35)$$

where $[J] = [\partial \Phi / \partial \xi]$, $[I]$ is the $N \times N$ identity matrix, and ξ denotes the property values at iteration i .

The value of ξ^* is usually fixed. However, in one variation of this procedure, ξ^* is set equal to the parameter distribution at the previous iteration, ξ_i . This variation is termed the Levenberg-Marquardt algorithm [1, 19, 20]. In this case, (2.35) simplifies to

$$[\mathbf{J}^T \mathbf{J} + 2\rho \mathbf{I}] \{\Delta \xi\} = [\mathbf{J}^T] \{\Phi_m - \Phi(\xi)\} \quad (2.36)$$

This method is of interest because it removes the penalty term from the gradient (i.e., the right-hand side of the equation).

In general, the convergence characteristics of the two approaches (i.e., conventional, as in (2.14)–(2.20), versus with Tikhonov regularization) are distinct and problem-specific [10, 21].

4.2 Hessian Scaling and Tikhonov Weight

The net effect of the regularization on the Hessian matrix $[\mathbf{J}^T \mathbf{J}]$ is to ensure its diagonal dominance, which facilitates its LU factorization [8]. However, determining the optimal weighting factor ρ is problem-specific and can be quite difficult [22, 23]. One complication is that the scale of the elements of the Hessian matrix can vary considerably from one imaging session to the next. A novel approach was developed by Joachimowicz and colleagues [21], who set ρ equal to the trace of the Hessian matrix multiplied by an empirically determined factor, α , and the relative least-square error at each iteration, e_{rel} :

$$\rho = \alpha e_{rel} \text{trace}([\mathbf{J}^T \mathbf{J}]) \quad (2.37)$$

Reducing the net regularization parameter as the iterations progress allows the influence of the less-dominant eigenvalues to be gradually introduced. That is, with large ρ at the algorithm's start, a blurred or smooth image is initially reconstructed; as ρ is reduced at each iteration, more detail appears (but the solution edges toward instability). The trace essentially measures the scaling effect of the matrix $[\mathbf{A}]$ on the vector $\{\Phi\}$ in (2.12) [8]. Therefore, the level of regularization can be controlled (to some degree) by the dimensionless quantity ρ .

One consequence of this approach is that since the Hessian diagonal terms can vary in magnitude, the influence of the regularization is uneven across the span of reconstruction parameters. Marquardt [20] introduced a matrix scaling (previously associated with the Levenberg regularization technique) that normalizes all Hessian diagonal terms to unity [19, 20]. Multiplying both sides of (2.18) by a diagonal matrix $[\mathbf{G}]$ and inserting the identity matrix (written as $[\mathbf{G}\mathbf{G}^{-1}]$) between the Hessian matrix $[\mathbf{J}^T \mathbf{J}]$ and the update vector $\{\Delta \xi\}$, we have

$$\left[\mathbf{G} \right] \left[\mathbf{J}^T \mathbf{J} \right] \left[\mathbf{G} \mathbf{G}^{-1} \right] \{ \Delta \xi \} = \left[\mathbf{G} \right] \left[\mathbf{J}^T \right] \{ \Phi^m - \Phi^c \} \quad (2.38)$$

which can be rewritten as

$$\left[\mathbf{G} \mathbf{J}^T \mathbf{J} \mathbf{G} \right] \{ \{ \mathbf{G}^{-1} \} \{ \Delta \xi \} \} = \left[\mathbf{G} \mathbf{J}^T \right] \{ \Phi^m - \Phi^c \} \quad (2.39)$$

and solved for $\{ \{ \mathbf{G}^{-1} \} \{ \Delta \xi \} \}$, which we will call $\{ \Delta \xi \}^*$. (Note that $\{ \Delta \xi \}$ itself can be easily recovered from $\{ \Delta \xi \}^*$, as $[\mathbf{G}]$ is diagonal.) The nonzero elements of $[\mathbf{G}]$ are chosen as

$$g_{ii} = \frac{1}{\sqrt{h_{ii}}} \quad (2.40)$$

where g_{ii} and h_{ii} are the diagonal elements of $[\mathbf{G}]$ and of the Hessian matrix $[\mathbf{J}^T \mathbf{J}]$, respectively. All diagonal entries of the scaled Hessian matrix $[\mathbf{G} \mathbf{J}^T \mathbf{J} \mathbf{G}]$ are unity, allowing for the level of regularization to be controlled by the addition to the diagonal of a single nondimensional quantity (e.g., λ). This quantity can be empirically chosen so that the algorithm is relatively robust across a broad span of imaging tasks.

4.3 Miscellaneous Techniques

We have utilized two additional techniques which generally act as forms of regularization. The first is a spatial filtering approach. When the property distribution is updated at each iteration, uneven fluctuations in the intermediate image can occur, especially during the early stages of the process. We have devised a spatial filter which can be applied through a matrix-vector multiplication that forms a weighted average of the value at node i with those of its surrounding neighbors [24]:

$$\xi_i^{\text{new}} = q \xi_i^{\text{old}} + \frac{(1-q)}{T} \sum_{j=1}^T \xi_j^{\text{old}} \quad (2.41)$$

Here, q is chosen to be between 0 and 1, T is the number of nodes to be averaged, and the superscripts “old” and “new” refer to the property values before and after application of the filter, respectively. As q varies from 1 to 0, the amount of filtering goes from none to full averaging with the T neighboring values.

Another technique is to reduce the iteration step size [25, 26]. Modifying (2.14) slightly produces

$$\{\xi\}_{i+1} = \{\xi\}_i + \tau\{\Delta\xi\} \quad (2.42)$$

where τ , which may be varied from 0 to 1, controls the step size.

It has been noted that in Newton iterative techniques, the computed update values can overshoot the desired values by a considerable margin, especially when the starting property distribution is not chosen carefully [11]. Reducing the step size may slow convergence, but is another useful tool for stabilizing an inherently unstable process.

5 3D IMAGING

In all of the imaging modalities discussed here, the physics of the electromagnetic wave propagation or mechanical vibration are intrinsically three-dimensional. To achieve 3D images is a sizeable computational task, especially given limitations on data acquisition and computational resources. Within each modality, therefore, we performed experiments to assess the image degradation to be expected from using approximate 2D algorithms. Results varied by modality. In MRE, it was found that a 2D approach was inadequate, while in MIS it was shown that 3D effects were greatly reduced by utilizing a low-contrast coupling medium (i.e., choosing a fluid bath with electrical properties as close as possible to those of the breast [27]).

In all four modalities, the ultimate goal is full 3D imaging. This can be achieved by incrementally perfecting tools for the 2D and 2.5D (hybrid of 2D and 3D) cases, and by designing these tools to be generalizable to fully 3D approaches. For example, the FE methods associated with the forward and inverse problems outlined in this chapter can be straightforwardly, albeit with effort, generalized to 3D. The degree to which 3D implementations are being explored for each modality is briefly discussed in the ensuing modality chapters.

6 CONCLUSION

This chapter has provided a brief overview of the iterative approach utilized in some form by all four imaging modalities treated in this book. It has outlined the basic notions of the inverse problem and highlighted issues such as computational cost and ill-conditioning. The dual mesh scheme, adjoint

method, and regularization strategies have been discussed, along with their implications for the imaging process. The methods outlined here are, however, by no means exhaustive or final.

The breast is a particularly intriguing imaging target for all four modalities because of its accessibility and relatively small volume. The complexity of the data acquisition systems required is not overly burdensome and the resources needed, even for the computationally intensive algorithms outlined here, are within reach.

REFERENCES

- [1] B. Kaltenbacher, "Newton-type methods for ill-posed problems." *Inverse Probl.*, Vol. 13, 1997, pp. 729–753.
- [2] A. Papoulis, *The Fourier Integral and Its Applications* (New York: McGraw-Hill, 1962).
- [3] R. F. Harrington, *Field Computation by Moment Methods* (Melbourne, FL: R. E. Krieger Publishing Co., 1968).
- [4] J. N. Reddy, *An Introduction to the Finite Element Method*, 2nd Ed. (New York: McGraw-Hill, 1993).
- [5] G. D. Smith, *Numerical Solution of Partial Differential Equations: Finite Difference Method* (Oxford: Clarendon Press, 1985).
- [6] A. Taflovie and S. Hagness, *Computational Electrodynamics: The Finite-Difference Time-Domain Method*, 2nd Ed. (Boston: Artech House, 2000).
- [7] K. D. Paulsen and W. Liu, "Memory and operations count scaling for coupled finite element and boundary element systems of equations." *Int. J. Numerical Methods in Eng.*, Vol. 33, 1992, pp. 1289–1304.
- [8] G. H. Golub and C. F. van Loan, *Matrix Computations*, 2nd Ed. (Baltimore, MD: Johns Hopkins Univ. Press, 1989).
- [9] T. B. A. Senior and J. L. Volakis, *Approximate Boundary Conditions in Electromagnetics* (London: Institution of Electrical Engineers, 1995).
- [10] P. M. Meaney, K. D. Paulsen, and T. P. Ryan, "Two-dimensional hybrid element image reconstruction for TM illumination." *IEEE Trans. Ant. and Prop.*, Vol. 43, 1995, pp. 239–247.
- [11] J. H. Mathews, *Numerical Methods for Mathematics, Science, and Engineering* (Englewood, NJ: Prentice-Hall, 1992).
- [12] K. D. Paulsen et al., "A dual mesh scheme for finite element based reconstruction algorithms." *IEEE Trans. Med. Imag.*, Vol. 14, 1995, pp. 504–514.
- [13] D. R. Lynch, K. D. Paulsen, and J. W. Strohbehn, "Finite element solution of Maxwell's equations for hyperthermic treatment planning." *J. Computational Physics*, Vol. 58(2), 1985, pp. 246–249.
- [14] Q. Fang et al., "Microwave image reconstruction from 3D fields coupled to 2D parameter estimation." *IEEE Trans. Med. Imag.*, 2004 (accepted).
- [15] P. M. Meaney, N. K. Yagnamurthy, and K. D. Paulsen, "Pre-scaling of reconstruction parameter components to reduce imbalance in image recovery process." *Physics Med. Biol.*, Vol. 47, 2002, pp. 1101–1119.
- [16] A. N. Tikhonov and V. Y. Arsenin, *Solutions of Ill-Posed Problems* (Washington, D.C.: Winston, 1977).

- [17] D. M. Pozar and D. H. Schaubert, *Microstrip Antennas: The Analysis of Microstrip Antennas and Arrays* (New York: Wiley-IEEE Press, 2001).
- [18] P. M. Meaney et al., "Microwave image reconstruction utilizing log-magnitude and unwrapped phase to improve high-contrast object recovery." *IEEE Trans. Med. Imag.*, Vol. 20, 2001, pp. 104–116.
- [19] K. Levenberg, "A Method for the solution of certain nonlinear problems in least squares." *Q. Appl. Math.*, Vol. 2, 1944, pp. 164–168.
- [20] D. W. Marquardt, "An algorithm for least-squares estimation of nonlinear parameters." *J. Soc. Ind. Appl. Math.*, Vol. 11, 1963, pp. 431–441.
- [21] N. Joachimowicz, C. Pichot, and J. R. Hugonin, "Inverse scattering: An iterative numerical method for electromagnetic imaging." *IEEE Trans. Antennas Propagat.*, Vol. 39, 1991, pp. 1742–1752.
- [22] P. M. Meaney et al., "A two-stage microwave image reconstruction procedure for improved internal feature extraction." *Med. Phys.*, Vol. 28, 2001, pp. 2358–2369.
- [23] D. Calvetti et al., "Tikhonov regularization and the L-curve for large discrete ill-posed problems." *J. Comput. Appl. Math.*, Vol. 123, 2000, pp. 423–446.
- [24] P. M. Meaney et al., "A two-stage microwave image reconstruction procedure for improved internal feature extraction." *Med. Phys.*, Vol. 28, 2001, pp. 2358–2369.
- [25] D. M. Bates and D. G. Watts, *Nonlinear Regression and Its Applications* (New York: Wiley, 1988).
- [26] G. F. F. Seber and C. J. Wild, *Nonlinear Regression* (New York: Wiley, 1989).
- [27] P. M. Meaney et al., "Importance of using a reduced-contrast coupling medium in 2D microwave breast imaging." *Int. J. Hyperthermia*, Vol. 19, 2003, pp. 534–550.

Alternative Breast Imaging

Four Model-Based Approaches

Paulsen, K.D.; Meaney, P.M.; Gilman, L. (Eds.)

2005, XVI, 254 p., Hardcover

ISBN: 978-0-387-23363-5